Numerical investigation on new configurations for vapor-phase aerosol reactors

G. Manenti, M. Masi*

Dipartimento di Chimica, Materiali e Ingegneria Chimica "Giulio Natta", Politecnico di Milano, Via Mancinelli 7, 20131 Milano, Italy

Received 2 September 2008
Received in revised form 23 April 2009
Accepted 28 April 2009
Available online 6 May 2009

1. Introduction

Producing fine ceramic powders in aerosol reactors by vapor phase represents today a competitive industrial process (Kodas and Hampden-Smith, 1999; Osterwalder et al., 2006). Micro- and nano-metal-oxide powders, like TiO_2, ZrO_2 or SnO_2, due to their chemical, optical and mechanical properties are used in a large range of advanced technological applications, such as components for laser devices, supports for catalysts or material for biomedical implants. For their production, the oxidation of metal-chlorides, $MeCl_4$, is an important synthesis route due to the high reactivity and relative low cost of precursors. High reactivity is determined by a fast chemical kinetics and by strong thermodynamic stability of monomer particles.

Chemical nucleation of ceramic particles is carried out in aerosol reactors where gaseous precursors are fed through separated nozzles. Depending on the fluid dynamics in the reaction volume, reactors may behave like continuous stirred reactors (CSR) or plug flow reactors (PFR). Practically, as the fluid-dynamic regime is typically turbulent, in particular near the nozzle region, their behavior is intermediate between that of the two previously mentioned reactors. This makes industrial aerosol reactor behavior strongly non-ideal and therefore difficult to be accurately designed. On the other hand, since dimensions and morphological–mechanical properties of metal-oxide particles depend on aerosol phenomena like nucleation and coagulation (i.e., by the local precursors concentration and by the so as-synthesized particles) residence times (i.e., reactor fluid dynamics) must be finely tuned to obtain a final product characterized by the required properties.

Because phenomena occurring at different spatial and time scales must be simultaneously handled, a multi-scale modeling approach is to be adopted. Nanometer dimensions characterize primary particles, whereas meters refer to reactor size: in the middle, there are several other scales, such as those inherent turbulence, micro-particles size and molecular gas path scales. Analogously, with reference to time scales, characteristic times of coagulation, sintering and other particle phenomena may correspond to microseconds, whereas industrial reactor residence times can be of order of seconds. In general, reactor macro-scale parameters, as operating conditions and geometry, must be linked to the chemical and physical phenomena occurring at particle scale.

Several researchers have dedicated works for simplifying and adapting the multi-scale approach to non-ideal reactors. In one of the first works, an isothermal laminar plug-flow reactor was modeled (Pratsinis et al., 1986) showing effects of the velocity profile on the particle concentration and size distribution. In other three pioneering studies (Schild et al., 1999; Tsantilis et al., 1999; Johannessen et al., 2000), the population balance equation (PBE), assuming a mono-dispersed distribution, was integrated by means of a commercial fluid dynamic code over energy and concentration fields for a laminar TiO_2 flame synthesis hot wall reactor, a palladium

* Corresponding author. Tel.: +39 02 2399 3131; fax: +39 02 2399 3180.
E-mail address: maurizio.masi@polimi.it (M. Masi).

nano-particle turbulent condenser and for an Al_2O_3 flame reactor, respectively. A fully coupled model, where the PBE was rewritten through the particle size distribution (PSD) moments and then was embedded into a commercial computational fluid dynamics (CFD) code, was applied for modeling an un-premixed 2D turbulent jet for the production of TiO_2 particles from tetra-isopropyl-orthotitanate ($Ti(OiPr)_4$) (Masi et al., 1999). Advances in aerosol simulation have led to more complex and accurate CFD models, like 3D modeling or application of alternative techniques for describing the particle evolution. Among them, a 3D turbulent mono-disperse model for a carbon black reactor (Skillas et al., 2005) and a quadrature method of moments for soot formation study in turbulent flames (Zucca et al., 2006) were presented.

In this work, a 3D aerosol CFD model, based on a mono-modal method of moments for the PBE and on the assumption of a log-normal PSD, was developed starting from a previous 2D model (Di Muzio et al., 2000). As a case study, the production of metal-oxide powders starting from the oxidation of $ZrCl_4$ by O_2 and $TiCl_4$ by H_2O was considered. In order to analyze the non-ideal behavior of relevant synthesis reactors, the aerosol model was coupled to momentum, energy and species balance equations by means of a commercial CFD code based on finite volume (FV) method. Accordingly, the three main statistical moments, the particle concentration, the volume and the spread of distribution, respectively, were embedded into the CFD code as scalar variables, generating three scalar balance equations.

To validate the model against experimental data, a laboratory scale ZrO_2 reactor and an industrial scale TiO_2 reactor were simulated to verify how simulations matched the as-synthesized particle size distribution. Because strong concentration and temperature gradients and consequently the most significant aerosol phenomena occur in the nozzle region, the CFD numerical investigations were focused on the nozzle configuration and on its impact on the final product quality. Modifying the arrangement of inlets, the nucleation and coagulation parameters change and consequently the aerosol evolution is modified. The impact of these reactor parameters were not investigated before in the literature. Numerical results showed that traditional axial-symmetric and jet-opposed nozzles may be characterized by a strong re-circulation. Accordingly, those inlets lead to a larger PSD than to the one that it could be obtained by a new, tangential arrangement where nozzle back-mixing phenomena are limited. This last configuration is firstly analyzed in this work.

2. Formulation of the aerosol CFD model

The population balance equation for an aerosol system in steady-state conditions is given by Eq. (1), where convective and diffusive particle transport, and nucleation and coagulation phenomena are represented by left-hand side and right-hand side terms, respectively (Friedlander, 1977; Ramkrishna, 2000). Other phenomena such as growth, sintering and breakage of particles are considered negligible in this work as particle surface reactions or gas condensation are not promoted in the investigated systems, sintering time is much longer than coagulation time and particles are of hard-agglomerate type, that is they do not experience breakage:

$$\boldsymbol{u}\cdot\nabla f(v)-\nabla\cdot(D_p\nabla f(v))=N+\frac{1}{2}\int_0^v \beta(v-v',v')f(v-v')f(v')\,dv' - \int_0^v \beta(v,v')f(v)f(v')\,dv' \quad (1)$$

The quantity $f(v)$ is the PSD based on the volume, representing the number of particles of volume v per unit of the reactor volume, $\beta(v,v')$ is the coagulation coefficient involving particles of volume v and v' and N is the nucleation rate. The second and the third term in the right-hand side of Eq. (1) are the gain and loss of particles due to coagulation, respectively. The most critical parameter to be defined is the coagulation coefficient as it depends on coagulation mechanism and on the particle transport regime. In case of binary interactions only and of Brownian diffusion, particle interactions can occur in two different regimes, free-molecular ($Kn \gg 1$, Kn = Knudsen number) or continuum ($Kn \ll 1$) regime, which expressions are given correspondingly in Eqs. (2) and (3) (Landgrebe and Pratsinis, 1989):

$$\beta_{FM}(v,v')=\left(\frac{3}{4\pi}\right)^{1/6}\left[\frac{6k_BT}{\rho_p}\left(\frac{1}{v}+\frac{1}{v'}\right)\right]^{1/2}(v^{1/3}+v'^{1/3})^2 \quad (2)$$

$$\beta_C(v,v')=\frac{2k_BT}{3\mu}\left[\frac{C_C(v)}{v^{1/3}}+\frac{C_C(v')}{v'^{1/3}}\right]^{1/2}(v^{1/3}+v'^{1/3}) \quad (3)$$

In the investigated systems, the mean particle diameter may fall within 0.1–0.3 μm: as it corresponds to a Knudsen's number close to unity, intermediate regimes may coexist and therefore an asymptotic combination of free-molecular and continuum boundary is usually adopted (Seinfeld, 1986). Furthermore, in turbulent fluid-dynamic regimes, where particle diameter is at least one order of magnitude larger than vortex diameter, the coagulation coefficient β is determined by the sum of Brownian and turbulent coagulation (Xiong and Pratsinis 1993a,b), that is $\beta=\beta_B+\beta_T$, where β_T is given by the following equation:

$$\beta_T(v,v')=2.3\left(\frac{3}{4\pi}\right)\sqrt{\frac{\varepsilon\rho}{\mu}}(v^{1/3}+v'^{1/3})^3 \quad (4)$$

In Eqs. (1)–(4) k_B, T, ρ, μ, ε are, respectively, the Boltzmann's constant, temperature, mass density, dynamic viscosity and turbulent dissipation rate of the process fluid, ρ_p is the particle density at the fluid temperature, and C_C and D_p are the Cunningham's factor and the particle diffusion coefficient, respectively (Hinds, 1982):

$$C_C(v)=1+2.257\cdot\left(\frac{k_BT}{\sqrt{2}\pi P d_C^2}\right)\cdot d_{gas}^{-1} \quad (5)$$

$$D_p=\frac{k_BTC_C}{3\pi\mu} \quad (6)$$

In vapor-phase oxidation of metal-chlorides, the particle nucleation rate N, coincides with the chemical reaction rate, R. Since TiO_2 and ZrO_2 metal-oxides are characterized by a very low vapor pressure and synthesized monomer particles present a diameter larger than the Kelvin's critical diameter (Friedlander, 1977), monomers can be considered thermodynamically stable (Ulrich et al., 1980). Describing the number of monomer particles of volume v_0 by a Dirac's function, δ, centered on v_0, the nucleation rate can be expressed as follows:

$$N(v)=N_{Av}R\delta(v-v_0) \quad (7)$$

where N_{Av} stays for the Avogadro's number.

The above equations enclose several variables and chemical–physical quantities. The gas velocity vector, $\boldsymbol{u}$, appears in the PBE, whereas Eqs. (2)–(6) depend on the operating conditions (temperature and pressure) and on the chemical–physical properties of the carrier fluid. Eq. (4) contains also a quantity related to turbulence. Finally, the expression of the chemical reaction rate, R, includes precursor concentrations. Consequently, it is necessary to link the PBE to relevant conservation equations for mass, momentum, energy and chemical species and to constitutive equations for other quantities. Considering Newtonian fluids and negligible pressure work and gravity field, conservation equations for a stationary system are

Table 1
Kinetics data for gas-phase reactions.

	Act. energy (kJ mol^{-1})	Freq. factor (dimensionless)	Chemical kinetic rate (kmol m^{-3} s^{-1})
$ZrCl_4$+O_2	$E \cong 126.3$	$k = 8.26\times10^4$	$K[ZrCl_4]\, e^{(-E/RT)}$
$TiCl_4$+2H_2O	$E \cong 0.0$	$k = 2.4\times10^{10}$	$K(T)^{1/2}[TiCl_4][H_2O]$

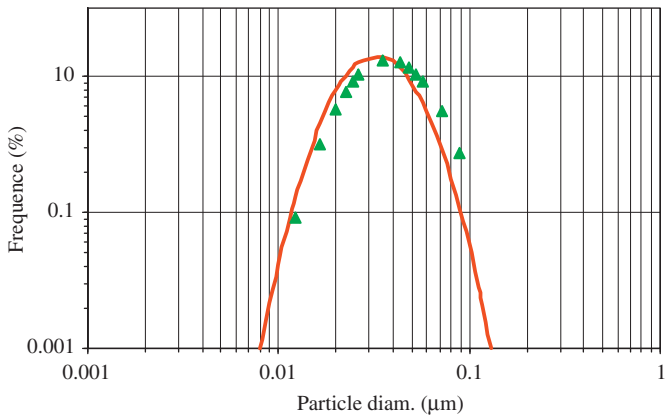

Fig. 1. Comparison between calculated PSD (line) and experimental PSD (symbols) for the ZrO_2 synthesis in a laboratory scale tubular reactor (Suyama et al., 1977).

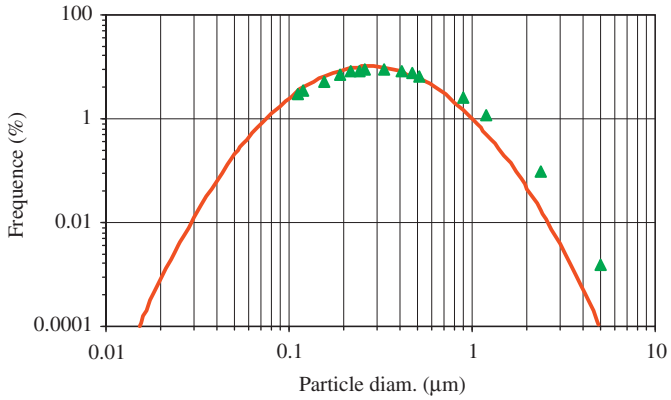

Fig. 2. Comparison between calculated PSD (line) and experimental PSD (symbols) for the TiO_2 synthesis in an industrial scale reactor (Manenti et al., 2006).

given by the following equations:

$$\nabla \cdot (\rho \boldsymbol{u}) = 0 \tag{8}$$

$$\nabla \cdot (\rho \boldsymbol{u} \cdot \boldsymbol{u}) = \nabla \cdot \Theta \tag{9}$$

$$\nabla \cdot (\rho \boldsymbol{u} H - \lambda \nabla \mathrm{T}) = S_H \tag{10}$$

$$\nabla \cdot [\rho \boldsymbol{u} \Phi - \rho \mathrm{D}_\Phi \nabla \Phi] = S_\Phi \tag{11}$$

The quantity Θ is the momentum stress tensor; H and Φ identify the fluid enthalpy and the concentration of any of the considered chemical species. Finally, λ and D are the thermal conductivity and mass diffusivity. Because the diluted conditions of the systems here discussed, the thermal conductivity can be approximated to that of the carrier gas, while a binary mass diffusivity between the species and the carrier gas can be used instead of the detailed expression derived by the Stefan–Maxwell equations (Carrà and Masi, 1998; Masi and Kommu, 2001). Finally, S represents the source terms due to the chemical reactions.

Eqs. (1) and (8)–(11) constitute a comprehensive aerosol model since chemical–physical phenomena are coupled to local velocity, temperature and concentrations. On the other hand, the resultant numerical system is computationally demanding, especially for large 3D geometrical domains. For the case of metal-oxide powders, the method of moments (Frenklach and Harris, 1987; Pratsinis, 1988) is functional for converting the above integral-differential PBE into a set of differential equations since, in accordance to experimental observations on the investigated systems, the PSD are of log-normal type and therefore their shape can be assumed a priori in the computational model:

$$f(v) = \frac{M_0}{3\sqrt{2\pi}\ln\sigma} \cdot \frac{1}{v} \cdot \exp\left[-\frac{\ln^2(v/v_g)}{18\ln^2\sigma}\right] \tag{12}$$

By the first three moments of the distribution, M_0, M_1 and M_2, the whole moment spectrum can be defined according to following relationships:

$$v_g = \frac{M_1^2}{M_0^{3/2} M_2^{1/2}} \tag{13}$$

$$\ln^2\sigma = \ln\frac{M_0 M_2}{M_1} \tag{14}$$

$$M_j = M_0 v_0^j \exp\left(\frac{j^2}{2}\right) \ln^2\sigma \tag{15}$$

where σ, v_g and j are, respectively, the geometric standard deviation, the mean particle volume and the generic moment. The first three moments are sufficient to characterize the aerosol dynamics and main particle properties, being their statistical significance corresponding to following physical quantities:

- M_0 is the particle concentration number, $N_p\ \mathrm{m}^{-3}$,
- M_1 is the particle volume number, $N_p\, m_p^3\ \mathrm{m}^{-3}$ and
- M_2 is the spread of particle distribution, or the polydispersity, $N_p\, m_p^3\ \mathrm{m}^3\ \mathrm{m}^{-3}$.

The particle mass, m_p, is assumed to be intrinsically conserved; therefore, rewriting the PBE by Eq. (11) and applying the method of moments, following balance scalar equations replace Eq. (1):

$$\begin{aligned}
&\nabla \cdot [\boldsymbol{u} M_0 - D_{M_0} \nabla M_0] = S_{M_0} \\
&\nabla \cdot [\boldsymbol{u} M_1 - D_{M_1} \nabla M_1] = S_{M_1} \\
&\nabla \cdot [\boldsymbol{u} M_2 - D_{M_2} \nabla M_2] = S_{M_2}
\end{aligned} \tag{16}$$

Representing the harmonic average on the coagulation coefficients for continuum and free-molecular regimes by Ξ and Ψ, the source terms in the above equations become:

$$S_{M_0} = N - \Xi M_0^2 \tag{17}$$

$$S_{M_1} = N v_0 \tag{18}$$

$$S_{M_2} = N v_0^2 - 2\Psi M_1^2 \tag{19}$$

Eq. (16) were inserted into the commercial CFD code as transport equations of the three user-defined scalar variables M_0, M_1 and M_2; both diffusivity coefficients and source terms were defined by means

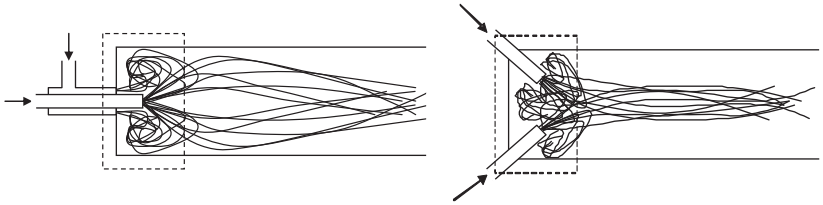

Fig. 3. Typical axial-symmetric (left) and jet-opposed (right) nozzle configurations. Recirculation zones are highlighted by dotted area.

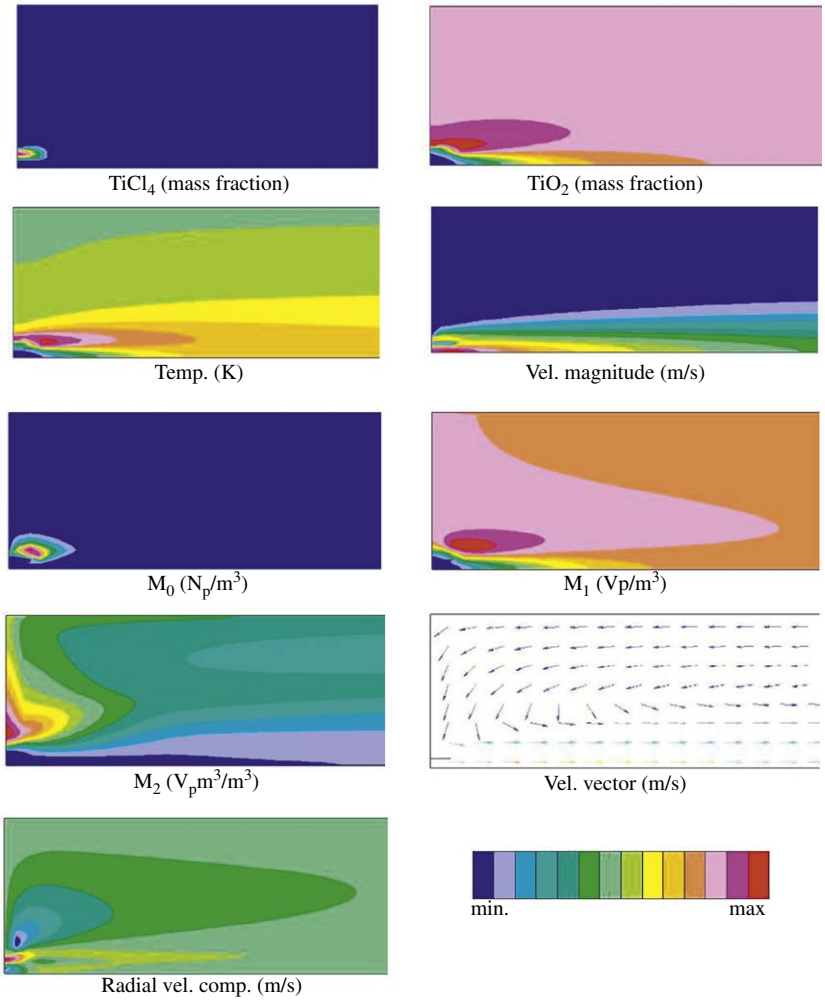

Fig. 4. CFD results for the first validating case (ZrO_2 reactor) axial mid-plane slice of the reactor.

of user-defined subroutines. In order to improve the numerical convergence, the high-order source terms (S , S_{M_0} and S_{M_2}) were linearized by a first-order Taylor's expansion. In agreement with the FV discretization method of the computational domain, they have been rearranged and implemented as follows (Patankar, 1980):

$$S_\Phi = S_{\Phi,n} V_n = S_{\Phi,nb} + S_{\Phi,n}\Phi_n = \left[S^0_{\Phi,n} - \left(\frac{dS_{\Phi,n}}{d\Phi} \right)^0 \Phi^0_n \right] V_n + \left(\frac{dS_{\Phi,n}}{d\Phi} \right)^0 V_n \quad (20)$$

where subscripts n and nb refer to the computational node and to neighbor nodes, respectively, the superscript 0 is related to the previous iteration, and V stays for the computational volume related to node.

Monitoring of aerosol properties during simulations and automatic generation of additional result files, like the PSD at the outlet of the reactor, was also necessary. Therefore, user-subroutines for tailored output were implemented in as well. In particular, the resulting computational particle size distribution was obtained by the mixing cup average value of the PSD, $f_{mix}(v)$, over the computational finite volumes V_i of the outlet region of the reactors, according to the following equation

$$f_{mix}(v) = \sum_{i=1}^{V_i} \frac{W_i}{W_{Tot}} \frac{M_0}{3\sqrt{2\pi}\ln\sigma} \cdot \frac{1}{v} \cdot \exp\left[-\frac{\ln^2(v/v_g)}{18\ln^2\sigma} \right] \quad (21)$$

Eq. (21), where W_i is the volumetric flow rate per distinct computational volume, allows the comparison between the calculated PSD

and the experimental one. At this point it is important to remark that, the monomodal implication for the PSD in any partitioned volume, it does not force the final size distribution of particles collected at reactor outlet to be monomodal as well, as already demonstrated in other systems (Di Muzio et al., 2000).

The aerosol CFD model constituted by Eqs. (7)–(11), Eq. (16) and constitutive equations for chemical–physical properties must be integrated with equations modeling turbulence. For this work, the robust and computationally light k–ε RANS model was adopted. The relevant built-in model available with the CFD code was used. Due to the fast, irreversible single-step reactions characterizing metal-oxide powder synthesis, the "eddy break-up" approach (Magnussen and Hjertager, 1976), built in the CFD code, was selected in combination with chemical kinetics: accordingly, the reaction time scale, τ_R, is obtained combining the turbulent time scale, $\tau_T = k/\varepsilon$, to the chemical time scale, $\tau_k = \Phi/R$, as $\tau_R = \tau_T + \tau_k$. In this way, the over-prediction of reaction rates in low-velocity zones is limited. Such an approach represents a good compromise between accuracy and CPU resources for simulation. Finally, with regard to the shear-induced coagulation coefficient given by Eq. (4), in the user-defined subroutines the local mean particle size is compared at each iteration to turbulence micro-scale, defined as $\eta = X \cdot Re^{-3/4}$. Practically, shear-induced coagulation coefficient is only accounted for when particle Stokes' number, St:

$$St = \frac{\rho_p d_p^2 u C_C}{18 \mu X} > 100 \tag{22}$$

The quantity X refers to the fluid-dynamic characteristic dimension which corresponds to nozzle diameter for the computational nozzle region and to the reactor diameter for other zones; Re stays for the Reynolds' number. Other details about the model can be found in Manenti (2007).

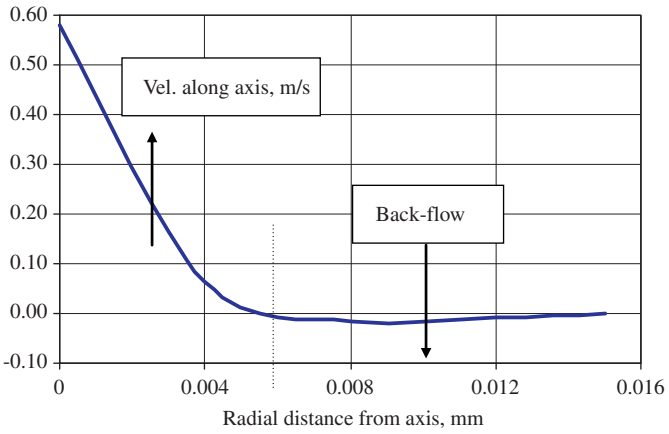

Fig. 5. Axial velocity profile against radial direction, at 15 mm from inlets.

3. Validation of the model

The aerosol model described above and implemented into the FV-CFD code was tuned with regard to the best turbulence parameters and numerical settings, and validated against two sets of experimental data. The former is inherent to a laboratory scale reactor described in literature while the latter refers to data collected from an industrial reactor. Because on-line monitoring and invasive measurements are difficult for aerosol reactors, model validation was based on the comparison of the calculated and experimental particle size distribution at the outlet of reactor when self-preserving conditions are reached. Validation based on mean particle diameter results effective as metal-oxide powders obtained from corresponding $MeCl_4$ precursors are experimentally log-normal distributed.

Although particle coagulation is modeled in the whole reactor bulk, this phenomenon is promoted in the very narrow zone of the flame only, as the bulk temperature for the investigated reactors is low; as a result, agglomeration of particles along the flow, and consequent fractality, is minor. Under this assumption, the coagulation rate can be deemed weakly sensitive to the fractal dimension of the particles (Vemury and Pratsinis, 1995) and therefore a spherical particle shape can be accounted for in the coagulation coefficient expressions, Eqs. (2)–(4). This is confirmed by TEM images of the laboratory scale reactor (Suyama et al., 1977), where particles present a low-open structure. However, models accounting for the particle fractality aspect have been already presented in the literature (Kruis et al., 1993).

The selected validating cases involve the oxidation of $ZrCl_4$ by O_2 in large stoichiometric excess and the hydrolysis of $TiCl_4$, according

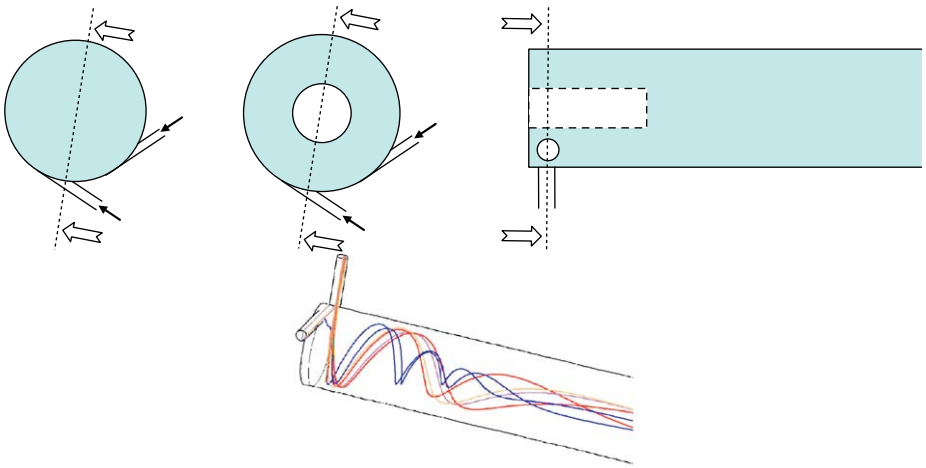

Fig. 6. Conceptual schemes for new aerosol nozzle configurations (top): tangential (left), annular-tangential (axial section—center, longitudinal section—right) and relevant helicoidally stream (bottom). Arrows and dotted line indicate slices for CFD results.

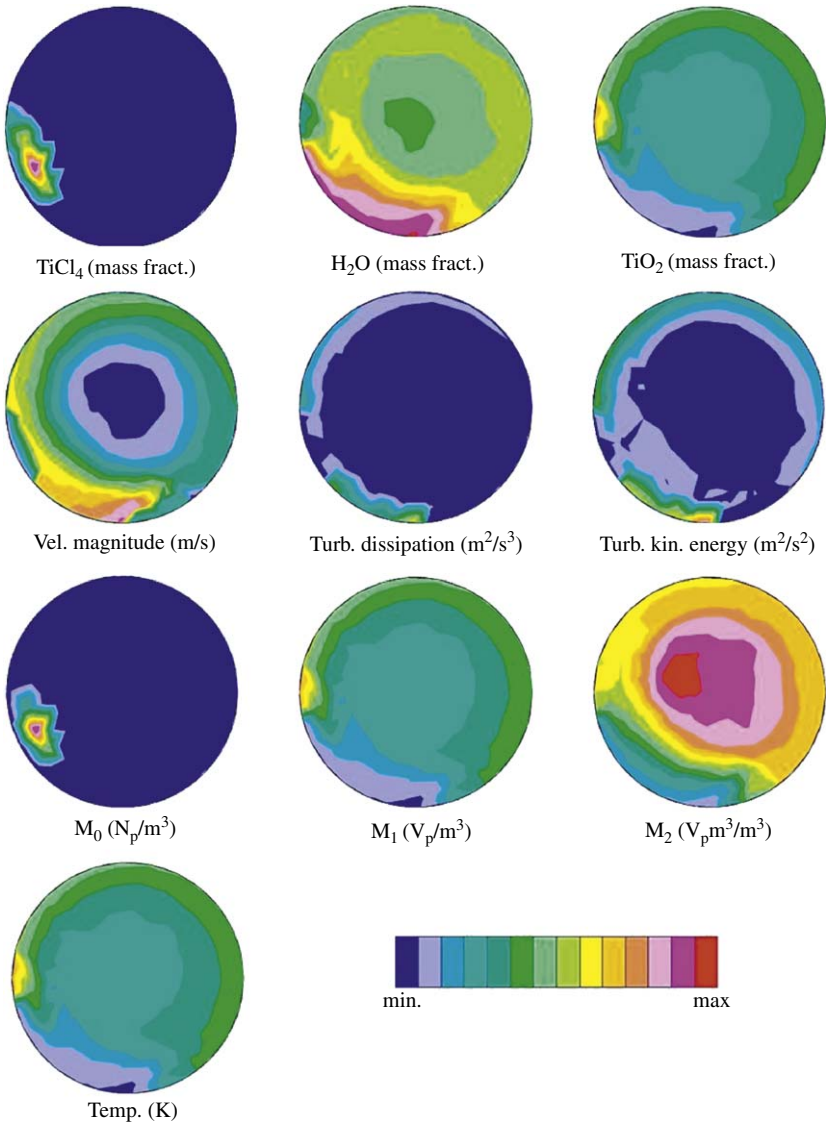

Fig. 7. Transversal sections of the inlet region of the industrial TiO_2 reactor rearranged with a tangential configuration (sections stay on the nozzles half plane).

Table 2
Maximum and minimum values for major quantities (perpendicular slices).

Quantity	Value
$TiCl_4$ mass fraction (dimensionless)	4.7×10^{-4} (local maximum value)
TiO_2 mass fraction (dimensionless)	0.005 (local maximum value)
M_0 (N_p m^{-3})	2.3×10^{25} (global maximum value)
M_1 (V_p m^{-3})	7.2×10^{-4} (global maximum value)
M_2 (V_p m^3 m^{-3})	2.1×10^{-26} (global maximum value)
Velocity (m s^{-1})	0.35 (local minimum value)
Temperature (K)	898 (global maximum value)

to reactions:

$$ZrCl_4 + O_2 \rightarrow ZrO_2 + 2Cl_2 \quad (23)$$

$$TiCl_4 + 2H_2O \rightarrow TiO_2 + 4HCl \quad (24)$$

whose reaction rate data are summarized in Table 1.

The activation energy and frequency factor for oxidation of $ZrCl_4$ were here estimated via collisional theory on the basis of $TiCl_4$ oxidation data (Pratsinis et al.,1990), whereas kinetics for hydrolysis of $TiCl_4$ was obtained by quantum-mechanical methods (Masi et al., 2001; Cavallotti et al., 2004).

The adopted data for Zirconia synthesis were obtained in a laboratory scale reactor with an axial-symmetric configuration, with concentric nozzles (Suyama et al., 1977). The reactor was 300 mm long, 30 mm I.D., with inner and outer nozzles of 4 and 8 mm I.D., respectively. Feed compositions (% vol.) were 0.4 for precursor (outer nozzle, at 533 K) and 54.3 for oxygen (inner nozzle, at 303 K), balanced with N_2 as carrier gas. As it can be observed by the data plotted in Fig. 1, the modeled PSD matches well with the experimental one. Particularly, the calculated particle geometric mean diameter was 0.043 μm against 0.053 μm of the as-synthesized experimental powder, being the geometric standard deviations 1.41 and 1.37, respectively.

The adopted data for TiO_2 synthesis were carried out in vertical industrial scale reactor characterized by a cylindrical body with a length to diameter ratio of 2.25 and by a reactor diameter to nozzles diameter ratio of 30. The reactor was conically terminated to collect particles through a fabric filter. The nozzle configuration was of jet-opposed type: the two reactants were separately injected by the two jets, placed on the reactor half plane and oriented towards the

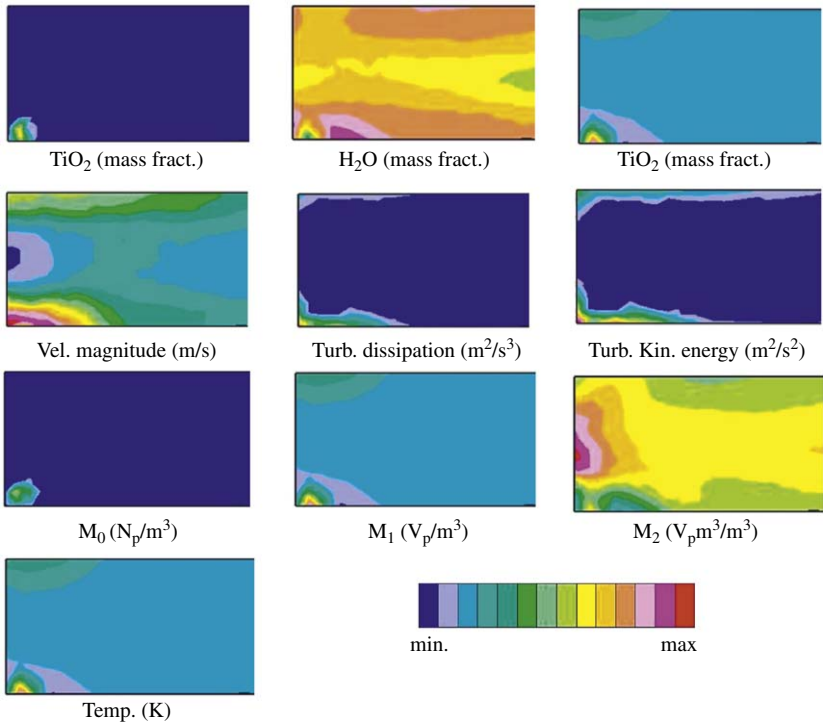

Fig. 8. Longitudinal sections of the inlet region of the industrial TiO_2 reactor rearranged with a tangential configuration (sections refer to the longitudinal half plane).

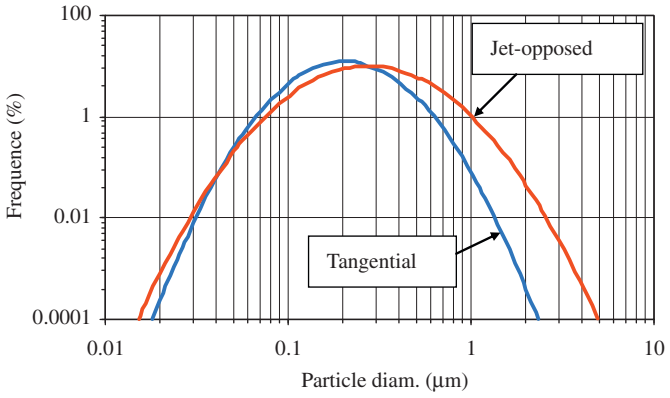

Fig. 9. Industrial TiO_2 reactor; comparison between PSD simulated with tangential and jet-opposed configuration.

reactor axis. This configuration leads to a large 3D computational domain as at least a half reactor is to be modeled. The industrial process was carried out at ambient pressure approximately, with a steam velocity at the nozzle tip of 10.5 m s^{-1}. $TiCl_4$, carried by Argon, was fed at 500 °C, with a nozzle tip velocity of 0.2 m s^{-1}. Reactor walls were kept at the constant temperature of 500 °C, which was about the same temperature of the bulk. Consequently, no significant wall deposition or thermophoretic effects were present. The comparison between simulated and industrial PSD is reported in Fig. 2, where the nice agreement between the two sets of data can be observed. In particular, simulated and industrial geometric mean diameters correspond to 0.271 and 0.305 μm, while geometric standard deviations are 1.83 and 1.96 μm, respectively. The examined reactor operated with a high load capacity and it was characterized by a strong recirculation (approx. the 15% of the mass flow), as demonstrated by the large spread of the experimental PSD. Those observations made the reactor interesting for additional simulations.

In conclusion, the developed model is able to simulate aerosol reactors of different scale and complexity. Thus it can be adopted to investigate reactor configurations not experimentally tested before with a quite acceptable level of reliability.

4. Limits of traditional nozzle configurations

Fluid mechanics to chemical reaction coupling constitutes a key aspect in non-ideal vapor-phase aerosol reactors modeling because reactants are usually fed in a segregated way and oxidation/hydrolysis reactions are fast compared to mixing. Furthermore, major aerosol phenomena take place in the nozzle region where highest temperatures and precursor concentration gradients occur. Consequently, the nozzle configuration requires an accurate and careful study.

A major limitation of traditional nozzles is due to the presence of recirculation zones near nozzle tips. This aspect was recently observed in aerosol reactors simulations (Skillas et al., 2005; Khalizov et al., 2006). As schematized in Fig. 3, both axial-symmetric nozzles and jet-opposed nozzles may generate backwards flows, which become important when closed bottom reactors are used, as in the present work. Such backward flows can lead to a poor product quality: the residence time of particles entrapped into recirculation vortex may be much longer than the required one and, moreover, such particles can be dragged into the flame zone. As a result, recirculated particles may abnormally grow or coagulate, producing a broader PSD, characterized by different morphological and optical properties with respect to the desired ones.

Such a limitation is clearly shown by the simulations reported in Fig. 4, inherent in the zirconia synthesis laboratory reactor analyzed here. $ZrCl_4$ reactant segregation and its instantaneous consumption are well evident. Maximum values for temperature (1429 K), ZrO_2,

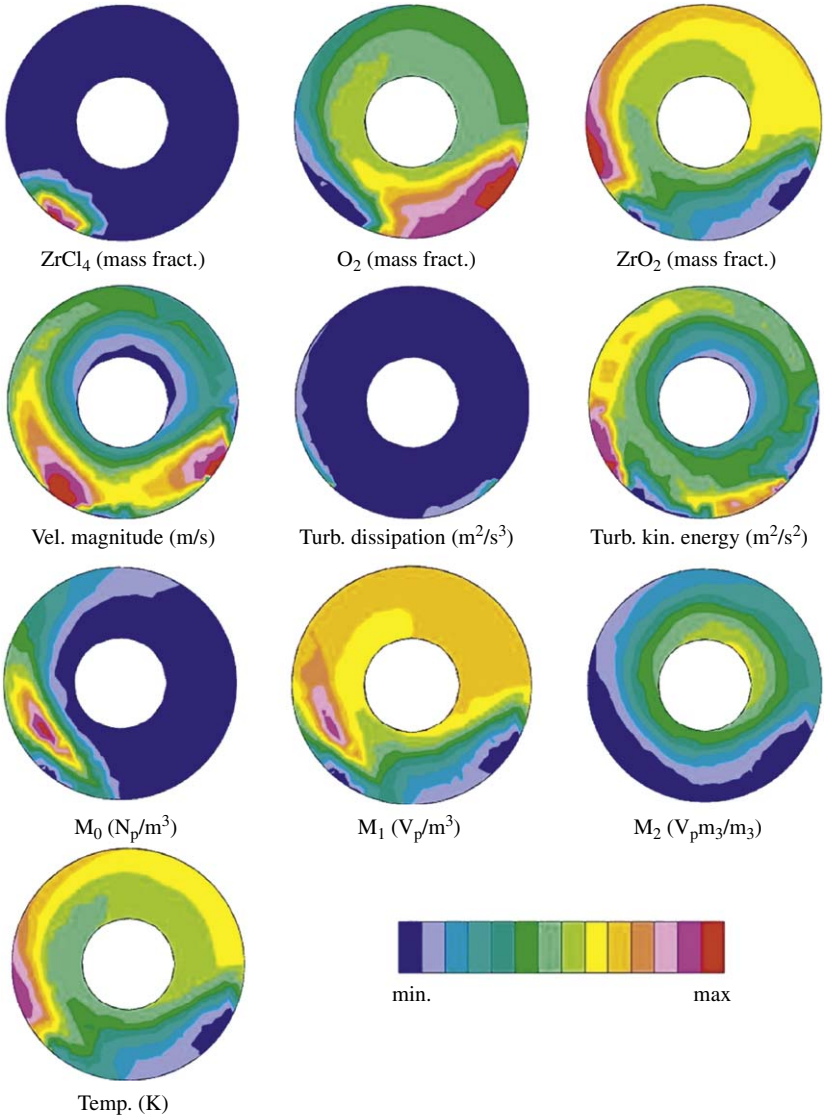

Fig. 10. Transversal slices of the inlet region for the ZrO_2 laboratory reactor with tangential-annular configuration (slices refer to the nozzles half plane).

M_0 and M_1 arise in the reaction zone, that is, in the particle nucleation region. Whereas highest values of the zero-order and first-order moments are directly linked to the reaction burst, highest values of second-order moment are linked to the simultaneous presence of primary and biggest particles. As maximum values of M_2 are predicted in the peripheral zone of the nozzle tips, it follows that back-mixing due to the axial-symmetric arrangement contributes to re-circulate as-synthesized particles. The velocity vector field clearly indicates a large reactor volume portion is interested by the back-flow. Further, the minimum value of the radial velocity ($-0.04\,m\,s^{-1}$) represents the main point where particles are re-circulated into the flame. Fig. 5 shows the inversion point of the axial velocity profile along radial direction. The back-flow reintroduces particles into the flame zone, where coagulation is thermodynamically and kinetically significant, therefore contributing to the enlargement of the particle size distribution.

5. Numerical investigation on new nozzle configurations

As the backward flow is the origin of high values of the second-order moment, that is of the broadening of the PSD, traditional nozzle reactor configurations have been rearranged into a tangential geometry illustrated in Fig. 6, while leaving unchanged the other process parameters, in particular the global residence time. By such an arrangement a helicoidally stream is obtained to limit macro-recirculation and stagnation zones. For the above industrial TiO_2 reactor, where a strong back-mixing arises, and for the laboratory ZrO_2 reactor a tangential nozzle and an annular-tangential nozzle configuration is adopted and then investigated, respectively.

For the TiO_2 reactor, the residence time (1.5 s), flow rates, precursor concentrations and temperatures were kept equal to those of the original design. The resulting 3D CFD model was constituted by 351 000 hexahedral cells; elapsed time per simulation extended to five days on a four-node cluster (HP-PA8700, 750 MHz). The simulation convergence was considered acceptable once global residuals and rate of change of dependent variables were below 10^{-3}. Furthermore, in order to save CPU time, nozzles were not simulated: a well-developed parabolic profile was then assumed at the inlet of the reactor.

In Fig. 7, qualitative contour plots for the central transversal section of the TiO_2 reactor nozzle inlets are reported, whereas relevant major values are given in Table 2.

By the results, it can be observed that the metal-chloride is immediately consumed and the reaction occurs without premixing. The global maximum value for the zero-order moment is located where the reaction takes place. Analogous contours are obtained for the synthesized powder, the temperature and the first-order moment. Highest kinetic turbulent energy and its dissipation are located in correspondence of reactor walls. Once again, the link between the velocity field and the second-order moment clearly appears: zones with high polydispersity correspond to zones with lowest values of gas velocity magnitude. This fact implies that particles remain entrapped in the stagnant zone, that is, in the reactor central core. Similar considerations can be drawn by the observation of the results plotted in Fig. 8, where longitudinal slices of the nozzle zone are illustrated. The reactant segregation local $TiCl_4$ mass fraction is again low; the stagnant zone and the correspondent high-value zone for second-order moment are evident. Nevertheless, the second-order moment is now lower than the original industrial reactor by five orders of magnitude, meaning that recirculation phenomena and related abnormal particle growth are limited. Effectiveness of tangential arrangement is confirmed by comparing PSD calculated with tangential and original nozzle configurations (Fig. 9). The geometric particle diameter and standard deviation reduce from 0.271 to 0.219 μm and from 1.83 to 1.65 μm, respectively. As a results, ceramic powder synthesized by the tangential reactor should be finer and of higher quality.

Following the results on the industrial TiO_2 reactor, a confirmation about efficiency of the tangential arrangement was investigated within the framework of the ZrO_2 laboratory reactor case. The residence time (58 s) and the inlet velocities were again kept equal to the original case. Accordingly with the previous case, nozzle piping was not modeled to keep the 3D model as computationally light as possible. However, in this case the tangential arrangement was modified by an annular space, installed at the inlet zone in order to avoid the central stagnant zone as illustrated in Fig. 6.

Figs. 10 and 11 report simulation results by transversal slices and longitudinal slices of the inlet region, respectively. Contour fields of dependent variables present the same trend of ones obtained for the TiO_2 reactor. Again, oxidation occurs in un-premixed conditions, with the metal-chloride totally consumed at the inlet. ZrO_2, M_0, M_1 concentrations and temperature present almost the same contour. As the maximum velocity is one order of magnitude lower than the industrial TiO_2 reactor; scalar fields are less stretched and turbulent kinetic energy and its dissipation is less pronounced. No significant difference is observed between maximum temperature, zero-order moment and first-order moment for axial-symmetric and tangential configuration. On the contrary, the second-order moment is lower for tangential nozzle arrangement, 3.1×10^{-24} $V_p\,m^3\,m^{-3}$, than the original one, 7.2×10^{-22} $V_p\,m^3\,m^{-3}$, and its high-value region is far from inlets.

In order to understand the peak of the second-order moment at the end of the annular section, the velocity vector field is zoomed in Fig. 12. As it can be noted, the M_2 behavior is again connected to the velocity map, more specifically to recirculation zones. The slice shows that there is a stagnant zone under and along the annulus (min/max local axial velocity for longitudinal slice are $0.02/0.18\,m\,s^{-1}$) and, furthermore, there is a back-flow, which is in any case smaller than in the axial-symmetric case.

Comparing the PSD obtained with axial-symmetric and annular-tangential configurations, Fig. 13, the effectiveness of tangential layout is confirmed: the geometric particle diameter and standard deviation decrease to 0.026 μm and 1.33 correspondingly. This should lead to a final ceramic powder of higher quality. In particular, the annular-tangential distribution shows that the biggest particles were cut since re-circulation effects are reduced. However, in this case the improvement is not much evident as the ZrO_2 laboratory reactor, on the contrary of the industrial one, does not present a strong back-flow and does not work at elevated capacity loads.

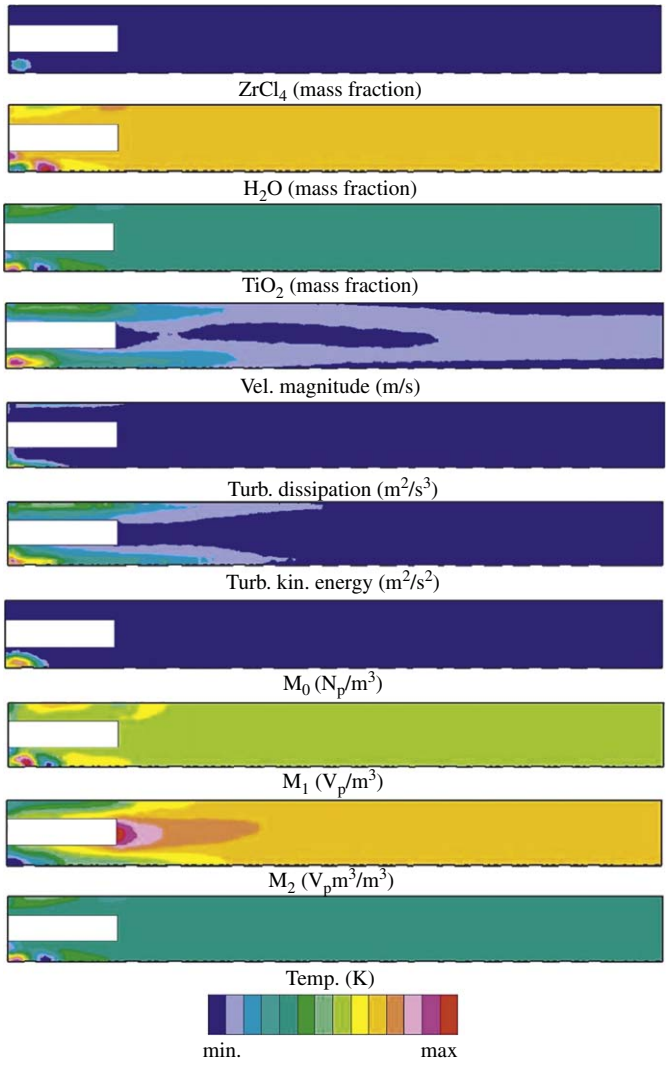

Fig. 11. Longitudinal slices of the inlet region for the ZrO_2 laboratory reactor with tangential-annular configuration (slices refer to the longitudinal half plane).

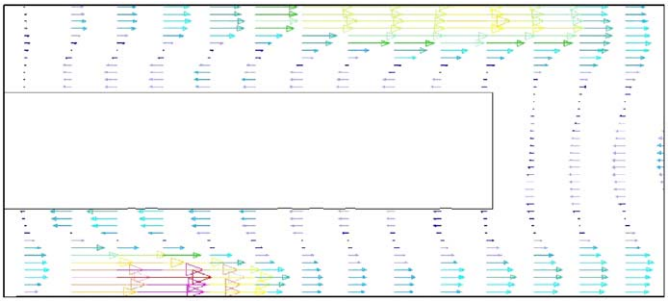

Fig. 12. Velocity field along the annulus (section refer to the longitudinal half plane).

6. Conclusions

A comprehensive and robust CFD model for the investigation and design of vapor-phase aerosol reactors was presented and discussed. Validation was carried out by comparing the computational and the

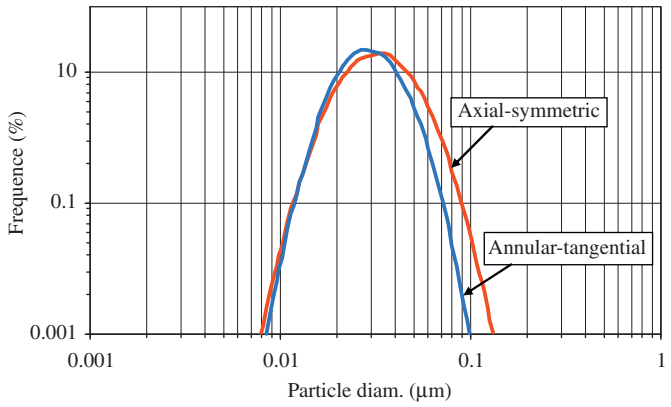

Fig. 13. Comparison of simulated PDF with annular-tangential and axial-symmetric configuration for the ZrO_2 reactor.

experimental PSD of two reactors, where metal-oxide fine powders, ZrO_2 and TiO_2, respectively, are synthesized starting from relevant metal-chlorides. The method of the moments and the assumption of a log-normal PSD were applied for reducing the PBE to more manageable differential equations. The resulting aerosol model was coupled to continuity, energy, momentum and chemical species conservative equations by means of user-defined sub-routines inserted into a commercial CFD code.

As nucleation and coagulation phenomena are predominant in the nozzle region, where temperature and concentration gradients are the highest, a detailed analysis of the nozzle arrangements has been performed and described. It has shown that traditional axial-symmetric and jet-opposed nozzle arrangements lead to a fluid-mechanics field characterized by recirculation patterns, which tend to broaden the spread of particle size distribution: accordingly, synthesized particle are back-dragged and trapped into vortex near the flame zone, where they may abnormally grow. This is evident by the second-order moment, representing the spread of the distribution, which presents its maximum values where vortex regions arise near flame.

In order to reduce back-mixing and over-coagulation phenomena, new aerosol reactor configurations have been investigated. Tangential and annular-tangential nozzle arrangements have been compared to the relevant axial-symmetric and jet-opposed geometries. Results show that the back-mixing flow rates and consequently the particle recirculation are reduced with new configurations, as the computational PSD are characterized by smaller polydispersities and mean geometrical particle diameters. This is promising from a technological and an industrial standpoint, as a product of higher quality may be synthesized.

Notation

Av	Avogadro number, N_p kmol^{-1}
Cu	Cunningham parameter, dimensionless
d	diameter, m or μm
E	chemical reaction activation energy, kJ mol^{-1}
f	particle size distribution function, N_p m^{-3}
H	static enthalpy, kJ mol^{-1}
j	generic moment
k_B	Boltzmann constant, J K^{-1}
K	frequency factor, dimensionless
Kn	Knudsen number, dimensionless
M_0	zero-order moment, N_p m^{-3}
M_1	first-order moment, V_p m^{-3}
M_2	second-order moment, V_p m^3 m^{-3}
N	particle nucleation, N_p s^{-1}
N_p	particle number, dimensionless
R	chemical kinetic rate, kmol s^{-1} m^3
Re	Reynolds number, dimensionless
St	Stokes number, dimensionless
S_Φ	source term for scalar quantity Φ, s^{-1}
T	temperature, K
$\boldsymbol{u}$	velocity vector, m s^{-1}
v	volume, m^3
v_0	monomer particle volume, m^3
v_g	geometric mean particle volume, m^3
V_p	total particle volume, m^3
W	flow rate, kg s^{-1}

Greek letters

β	coagulation coefficient, m^3 N_p^{-1} s^{-1}
δ	Dirac function, dimensionless
ε	turbulent dissipation rate, m^2 s^{-3}
η	turbulence scale, m
κ	turbulent kinetic energy, m^2 s^2
λ	thermal conductivity, W m^{-1} K^{-1}
μ	dynamic viscosity, kg s^{-1} m^{-1}
Ξ	coagulation coefficient, m^3 N_p^{-1} s^{-1}
ρ	density, kg m^{-3}
σ	geometric standard deviation, dimensionless
τ	characteristic time, s
Φ	scalar quantity
Ψ	coagulation coefficient, m^3 N_p^{-1} s^{-1}

Subscripts

K	relative to chemical reaction
n	relative to computational node n
p	relative to particle
t	relative to turbulence

Superscripts

0	relative to initial or previous temporal step
j	relative to generic moment j

References

Carrà, S., Masi, M., 1998. Kinetic approach to material synthesis by gas phase deposition. Progress in Crystal Growth and Characterization of Materials 37, 1–46.

Cavallotti, C., Moscatelli, D., Masi, M., Carrà, S., 2004. Accelerated decomposition of gas phase metal organic molecules determined by radical reactions. Journal of Crystal Growth 266, 363–370.

Di Muzio, F., Masi, M., Carrà, S., 2000. Modeling of aerosol deposition of titania thin films. Materials Chemistry and Physics 66, 286–293.

Frenklach, M., Harris, S.J., 1987. Aerosol dynamics modeling using the method of moments. Journal of Colloid and Interface Science 118, 252–261.

Friedlander, S.K., 1977. Smoke Dust and Haze. Wiley Interscience, New York.

Hinds, W.C., 1982. Aerosol Technology. Wiley Interscience, New York.

Johannessen, T., Pratsinis, S.E., Livbjerg, H., 2000. Computational fluid particle dynamics of flame synthesis of alumina particles by coagulation and sintering. Chemical Engineering Science 55, 177–191.

Khalizov, A.F., Earle, M.E., Johnson, W.J.W., Stubley, G.D., Sloan, J.J., 2006. Modeling of flow dynamics in laminar aerosol flow tubes. Aerosol Science 37, 1174–1187.

Kodas, T.T., Hampden-Smith, M.J., 1999. Aerosol Processing of Materials. Wiley-VCH, New York.

Kruis, F.E., Kusters, K.A., Pratsinis, S.E., Scarlett, B., 1993. A simple model for the evolution of the characteristics of aggregate particles undergoing coagulation and sintering. Aerosol Science and Technology 19, 514–526.

Landgrebe, J.D., Pratsinis, S.E., 1989. Gas phase manufacture of particulates: the interplay of chemical reaction and aerosol coagulation in the free molecular regime. Industrial & Engineering Chemistry Research 28, 1474–1481.

Magnussen, B.F., Hjertager, B.H., 1976. On mathematical modeling of turbulent combustion with special emphasis on soot formation and combustion. In: 16th Symposium (International) on Combustion, The Combustion Institute, pp. 719–729.

Manenti, G., 2007. Synthesis of ceramic powders by vapor phase: innovative configurations for aerosol reactors. Ph.D. Thesis, Politecnico di Milano, Italy.

Manenti, G., Di Muzio, F., Masi, M., 2006. A comprehensive multi-scale approach for vapor-phase synthesis of metal oxide particles. In: Wesseling, P., Oñate, E., Périaux, J. (Eds.), Proceedings of European Conference on Computational Fluid Dynamics ECCOMAS CDF 2006, TU Delft, Delft, The Netherlands. 14 Manenti, G., Di Muzio, F., Masi, M., 2006. A comprehensive multi-scale approach for vapor-phase synthesis of metal oxide particles. In: Wesseling, P., Oñate, E., Périaux, J. (Eds.), Proceedings of European Conference on Computational Fluid Dynamics ECCOMAS CDF 2006, TU Delft, Delft, The Netherlands.

Masi, M., Kommu, S., 2001. Epitaxial reactor modeling. In: Crippa, D., Masi, M., Rode, D.L. (Eds.), Silicon Epitaxy. Academic Press, San Diego, CA, pp. 185–224 (Chapter 6).

Masi, M., Di Muzio, F., Brigante, P., Grimaldi, M., Carrà, S., 1999. Modeling of aerosol reactor for synthesis of TiO_2 powder. In: Proceedings of ICheaP-4, AIDIC Conference, Milan, p. 612.

Masi, M., Di Muzio, F., Carrà, S., 2001. CFD modeling of aerosol reactors for materials synthesis. In: Electrochemical Society Symposium Series, vol. 13, pp. 488–495.

Osterwalder, N., Capello, C., Hungerbuhler, K., Stark, W.J., 2006. Energy consumption during nanoparticle production: How economic is dry synthesis? Journal of Nanoparticle Research 8, 1–9.

Patankar, S.V., 1980. Numerical Heat Transfer and Fluid Flow. Hemisphere, Taylor & Francis, New York.

Pratsinis, S.E., Bai, H., Biswas, P., Frenklach, M., Mastrangelo, S.V.R., 1990. Kinetics of titanium (VI) chloride oxidation. Journal of American Ceramic Society 73, 2158–2162.

Pratsinis, S.E., Kodas, T.T., Dudukovic, M.P., Friedlander, S.K., 1986. Aerosol reactor design: effect of reactor type and process parameters on product aerosol characteristics. Industrial & Engineering Chemistry Process Design and Development 25, 634–642.

Pratsinis, S.E., 1988. Simultaneous nucleation, condensation, and coagulation in aerosol reactors. Journal of Colloid and Interface Science 124, 416–427.

Ramkrishna, D., 2000. Population Balances. Academic Press, London.

Seinfeld, J., 1986. Atmospheric Chemistry and Physics of Air Pollution. Wiley Interscience, New York.

Schild, A., Gutsch, A., Muhlenweg, H., Pratsinis, S.E., 1999. Simulation of nanoparticle production in premixed aerosol flow reactors by interfacing fluid mechanics and particle dynamics. Journal of Nanoparticle Research 1, 305–315.

Skillas, G., Becker, C., Muhlenweg, H., Behnisch, J., 2005. Simulation of particulates in a carbon black reactor. Journal of Nanoparticle Research 7, 15–27.

Suyama, Y., Mizobe, T., Kato, A., 1977. ZrO_2 powders produced by vapour phase reaction. Ceramurgia International 3, 141–146.

Tsantilis, S., Pratsinis, S.E., Haas, V., 1999. Simulation of synthesis of palladium nanoparticles in a jet aerosol flow condenser. Journal of Aerosol Science 30, 785–803.

Ulrich, L., Cheng, R.K., Schefer, R.W., Willes, D.R., 1980. Thermophoresis of particles in a heated boundary layer. Journal of Fluid Mechanics 101, 737–743.

Vemury, S., Pratsinis, S.E., 1995. Self-preserving size distributions of agglomerates. Journal of Aerosol Science 26, 175–185.

Xiong, Y., Pratsinis, S.E., 1993a. Formation of agglomerate particles by coagulation and sintering—part I. A two-dimensional solution of the population balance equation. Journal of Aerosol Science 24, 283.

Xiong, Y., Pratsinis, S.E., 1993b. Formation of agglomerate particles by coagulation and sintering—part II. The evolution of the morphology of aerosol-made titania, silica and silica-doped titania powders. Journal of Aerosol Science 24, 301.

Zucca, A., Marchisio, D.L., Barresi, A.A., Fox, R.O., 2006. Implementation of the population balance equation in CFD codes for modelling soot formation in turbulent flames. Chemical Engineering Science 61, 87–95.